Article

Crystallization of Secondary Phase on Super-Duplex Stainless Steel SAF2507: Advanced Li-Ion Battery Case Materials

Byung-Hyun Shin [1], Dohyung Kim [2,*] and Jang-Hee Yoon [1,*]

1   Busan Center, Korea Basic Science Institute, Busan 46742, Republic of Korea; lemonhouse211@kbsi.re.kr
2   Innovative Graduate Education Program for Global High-Tech Materials and Parts, Busan 46241, Republic of Korea
*   Correspondence: dhkim@pusan.ac.kr (D.K.); jhyoon@kbsi.re.kr (J.-H.Y.); Tel.: +82-51-510-1498 (D.K.); +82-51-974-6140 (J.-H.Y.)

Abstract: The demand for Li-ion batteries has increased because of their extensive use in vehicles and portable electronic devices. This increasing demand implies greater interaction between batteries and humans, making safety a paramount concern. Although traditional batteries are fabricated using Al, recent efforts to enhance safety have led to the adoption of AISI304. The strength and corrosion resistance of AISI304 are greater than those of Al; however, issues such as stress-induced phase transformation and low high-temperature strength have been observed during processing. Duplex stainless steel SAF2507, which is characterized by a dual-phase structure consisting of austenite and ferrite, exhibits excellent strength and corrosion resistance. Although SAF2507 demonstrated outstanding high-temperature strength up to 700 °C, it precipitated a secondary phase. The precipitation of this secondary phase, believed to be caused by the precipitation of the carbides of Cr and Mo, has been extensively studied. Research on the precipitation of the secondary phase near 1000 °C has been conducted owing to the annealing temperature (1100 °C) of the SAF2507 solution. The secondary phase precipitates at approximately 1000 °C because of slow cooling rates. However, few studies have been conducted on the precipitation of the secondary phase at approximately 700 °C. This study analyzed the precipitation behavior of the secondary phase at 700 °C when SAF2507 was applied and assessed its safety during heat generation in Li-ion batteries. The precipitation behavior was analyzed using field emission scanning electron microscopy for morphology, energy-dispersive X-ray spectroscopy for composition, and X-ray diffraction for phase identification.

Keywords: Li-ion battery case; super duplex stainless steel; secondary phase; temperature effect

1. Introduction

Increasing demand for electric vehicles and portable electronic devices has resulted in increasing demand for Li-ion batteries. Because Li-ion batteries generate heat during usage, with temperatures reaching up to 700 °C [1–3], numerous studies have been conducted to ensure safety. Previous studies have focused on suppressing heat generation to control this exothermic reaction. Rahman and Lin designed a system to monitor battery temperature for heat control, whereas Klink et al. employed sensor- and model-based thermal runaway modeling techniques [2,4]. Although studies such as those previously mentioned aim to detect and alert users to early heat generation, its delay cannot be prevented once the reaction begins. Therefore, systems for suppressing explosions at high temperatures have been developed to enhance safety. However, fundamental safety issues at high temperatures remain unresolved. Recently, Li-ion battery casing materials have changed from Al to AISI304 (austenite stainless steel) owing to their higher strength and corrosion resistance [5–7].

AISI304 is an austenitic stainless steel with excellent strength and corrosion resistance [8–10]. However, concerns arise owing to its low strength at high temperatures

(170 MPa at 700 °C) and martensitic transformation (from face-centered cubic (FCC) to base-centered tetragonal (BCT)) under stress. Its low strength at high temperatures is attributed to the high alloy content and unstable phase transformations at high temperatures. Martensitic transformation occurs when stressed, unstable austenite cooled after solution treatment undergoes hardening, leading to decreased strength and corrosion resistance. Additionally, the high thermal expansion coefficient of AISI304 (16.6×10^{-6} ppm/°C) accelerates corrosion at high temperatures and reduces strength. Since it was extensively studied in the early 1990s, AISI304 remains widely used because of its widespread recognition as a highly corrosion-resistant and high-strength material.

The selection of materials for battery cases is crucial to achieving excellent strength and corrosion resistance [11–13]. Stainless steel exhibits excellent strength and corrosion resistance, although its specific characteristics vary depending on its type. Stainless steels are categorized based on their main phases, including austenitic, ferritic, martensitic, and duplex stainless steels (DSS). Austenitic stainless steels offer superior corrosion resistance but low strength at high temperatures. Ferritic and martensitic stainless steels exhibit high strength and high-temperature strength but low corrosion resistance. In contrast, DSS, composed of both austenite and ferrite phases, demonstrates excellent strength and corrosion resistance. However, because of the precipitation of a secondary phase at high temperatures, further research on this material is necessary before it can be used. DSS can enhance the safety of Li-ion batteries; however, further research is necessary in this regard.

To improve safety, a stainless steel with high corrosion resistance and high-temperature strength, such as DSS, is required [14,15]. Super DSS (SDSS), represented by SAF2507, consists of austenite and ferrite phases and provides high strength and corrosion resistance. SAF2507 falls under the grade 42 classification in the pitting resistance equivalency index and exhibits superior strength, corrosion resistance, high-temperature strength (exceeding 300 MPa at 700 °C), and a low coefficient of thermal expansion (13.5×10^{-6} ppm/°C). These properties enhance the safety of Li-ion battery casings. However, despite extensive studies on marine plant applications, research on the processing and coating of SDSS remains insufficient.

Although SAF2507 exhibits high-temperature strength, concerns arise owing to the precipitation of secondary phases, which result in alloy inhomogeneity and decreased corrosion resistance. Nillson and Tan analyzed the corrosion resistance and phase fraction changes with heat treatment in SAF2507 [14]. Martins analyzed the microstructure of cast SAF2507 [16]. Although the microstructure and corrosion resistance of SAF2507 have been extensively studied, research on the precipitation behavior of secondary phases at approximately 700 °C and its effect on alloy distribution is limited. Therefore, before SAF2507 can be applied to Li-ion battery casings, the precipitation of secondary phases must be understood because it significantly affects the properties of materials near 700 °C.

This study analyzed the influence of the chemical composition after heat treatment and examined the behavior of the secondary phases. SAF2507 was fabricated via casting and subsequently subjected to heat treatment at 1100 °C. The crystallization and precipitation morphology of secondary phases at 700 °C were observed over time; additionally, the growth of secondary phases under Li-ion battery usage conditions was observed using field emission scanning electron microscopy (FE-SEM). Furthermore, the changes in the chemical composition and phases were analyzed using energy-dispersive X-ray spectroscopy (EDS) and X-ray diffraction (XRD).

2. Materials and Methods

2.1. Materials

SAF2507 (manufactured by POSCO SS, Changwon, Republic of Korea) was used in this study. The chemical composition of cast SAF2507 was analyzed using inductively coupled plasma mass spectrometry (ICP-MS, Thermo Fisher Scientific, Waltham, MA, USA); the results are presented in Table 1. The pitting resistance equivalent number (PRE), which was indicative of corrosion resistance and calculated using Equation (1), was 42 [14]. Stainless

steel inherently enhances corrosion resistance owing to the formation of a passivation layer primarily composed of Cr_2O_3. Cr acts as the major component of the Cr_2O_3 layer, whereas Mo induces stress in Cr-deficient areas, aiding in the formation of the passive layer. N is an interstitial element that enhances the corrosion resistance of the passive layer at grain boundaries [17,18].
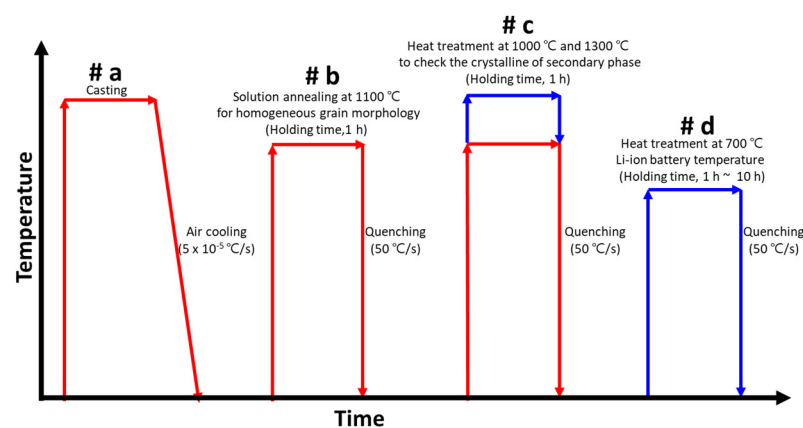
Pitting resistance equivalent number (PRE) = wt.% Cr + 3.3 wt.% Mo + 16 wt.% N (1)

Table 1. Chemical composition of super-duplex stainless steel SAF2507 by ICP-MS for advanced Li-ion battery case material.

Elements	C	N	Mn	Ni	Cr	Mo	Cu	Fe
Chemical composition, wt.%	0.01	0.27	0.8	6.8	25.0	3.8	0.2	Bal

2.2. Heat Treatment

A schematic of the heat treatment conditions is shown in Figure 1. To observe the crystallization, growth, and characteristics of the secondary phase, the specimens were annealed at 1000 °C for 1 h, then cooled at a rate of 50 °C/s. Castings solidify at high temperatures before being air-cooled; this makes them ideal for observing the crystallization phases [19–21]. The microstructure after casting and after heat treatment at 1100 °C was assessed to determine the recrystallization behavior of the phases of austenite and ferrite. Heat treatment was performed at 1100 °C because this temperature equilibrates the fractions of austenite and ferrite and achieves the highest corrosion resistance. After heat treatment, the morphology and state of the secondary phase were examined at 1000 °C. The secondary phase crystallizes and precipitates at temperatures below 1020 °C. The segregation of the chemical composition also occurs because of the increasing volume fraction of austenite (transformation from ferrite), which is known to cause secondary-phase crystallization. A subsequent heat treatment was performed to observe the precipitation behavior of the secondary phase. Specimens were heat-treated at 1300 °C to induce ferritization and observe the growth of austenite and the secondary phase. Subsequently, the specimens were heat-treated for 0–10 h at 700 °C to investigate the phase transformations during the ignition of the cases of Li-ion batteries; cooling was conducted at 50 °C/s.

Figure 1. Schematic diagram of heat-treatment condition of super-duplex stainless steel SAF2507 (Red line is the precipitation condition on manufacturing process, and blue line is the condition to check the precipitation of secondary phase on work of Li-ion battery case).

2.3. Microstructure and Phase

The microstructure was examined using FE-SEM (SUPRA 40VP system, Zeiss, Land Baden-Württemberg, Germany) based on the heat-treatment schematic depicted in Figure 1. The post-cast uneven microstructure was homogenized by annealing at 1000 °C [19,22,23].

Subsequently, the precipitation behavior of the secondary phase was observed. The red line in Figure 1 represents the typical annealing conditions, illustrating the precipitation behavior of the secondary phase after annealing. The blue line represents conditions for investigating the microstructure at the fever temperature of the cases of Li-ion batteries; the temperature of the ferrite fraction increased to 1300 °C. Thereafter, the crystallization behavior of the secondary phase was observed at 700 °C over varying annealing times. The crystallized phases were confirmed using XRD (D8 VENTURE, Stanford, CA, USA), and the phase fractions were analyzed according to ASTM E 1245 [22,24,25]. Volume fraction analysis was conducted at ×200 magnification seven times; the mean was calculated using the median of five values. For the phase and volume fraction analyses, etching was performed using a 10 wt.% NaOH electrolyte solution at 5 V for 30 s.

2.4. Chemical Composition

After casting, the microstructure exhibited irregular austenite formation with crystallization and secondary-phase growth at the austenite boundaries. The chemical composition of heat-treated SAF2507 was analyzed using EDS (SUPRA 40VP system, Zeiss, Land Baden-Württemberg, Germany); the results are presented in Table 2. Austenite and ferrite display differences in their chemical compositions, particularly in those of Cr and Mo [26,27]. Austenite is characterized by high levels of Ni, Mn, and N, which are typical stable FCC elements. Conversely, ferrite exhibited elevated levels of Cr and Mo, which are typical BCC-stabilizing elements. Because N is an interstitial element, its quantification using EDS is challenging. Therefore, N was quantified as follows: the maximum quantity of N that was soluble in ferrite was 0.05 wt.%, with the remainder dissolved in austenite. Despite containing low Cr and Mo contents, austenite maintained excellent passivity because of its high N solubility, whereas ferrite reinforced passivity in the presence of Cr and Mo.

$$N_r = \text{chemical composition of } N_{\text{Total}} \text{ wt.\%} - \text{Ferrite}_{\text{VF}} \times 0.05 \text{ wt.\%} \tag{2}$$

Table 2. Chemical composition of austenite and ferrite after heat treatment at 1100 °C on super-duplex stainless steel SAF2507. Unit: wt.%.

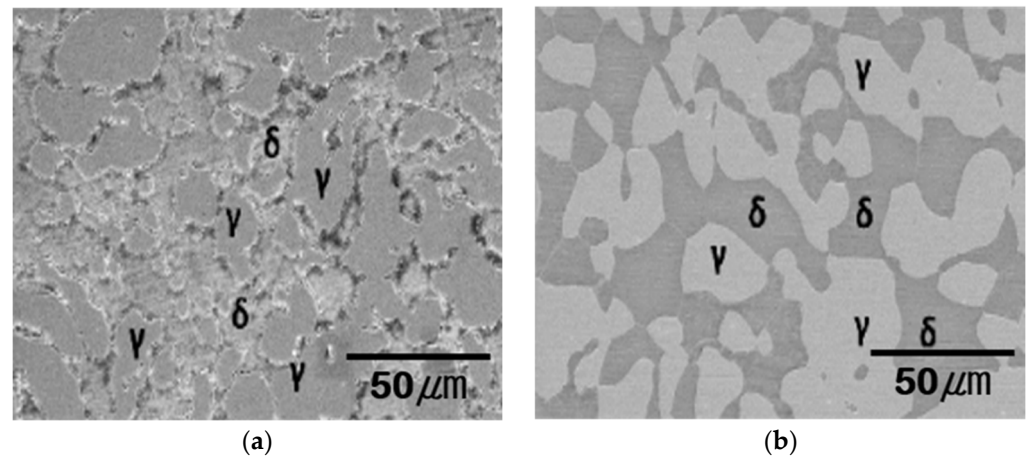| Elements	C	N	Mn	Ni	Cr	Mo	Fe	PRE
Austenite	0.01	0.51	1.1	7.9	23.3	3.2	Bal	42.0
Ferrite	0.01	0.05	0.8	5.5	26.6	4.4	Bal	42.1

3. Results

3.1. Heat Treatment

Owing to its high-alloy chemical composition, SAF2507 is adjusted and cast in electric furnaces [28,29]. In this study, SAF2507 castings produced in an electric furnace were used. The casting was performed at temperatures exceeding 2000 °C, resulting in liquid-to-solid phase transformations. Owing to the differences in cooling rates between the interior and exterior of the casting, the molten metal was poured into a mold and rapidly cooled by air or water. Figure 2a,b show the microstructures after casting and after heat treatment at 1100 °C, respectively. The austenite morphology of the cast SAF2507 exhibited an irregular grain morphology and contained less than 1% secondary phase. Following annealing at 1100 °C, the uniformity of the microstructure of SAF2507 increased, and it exhibited an austenite-to-ferrite ratio of 5:5, which was the highest corrosion-resistant condition.

Table 2 lists the chemical composition of SAF2507 after heat treatment at 1100 °C (solution-annealing condition). Following heat treatment, the chemical compositions of the austenite and ferrite phases of SAF2507 were compared. Austenite comprised 7.9 wt.% Ni, 1.1 wt.% Mn, and 0.51 wt.% N [30,31]. In contrast, ferrite consisted of 26.6 wt.% Cr, 4.4 wt.% Mo, and 0.05 wt.% N. These differences in alloy composition result in variations in the stabilizing elements based on the lattice structure of each phase. This
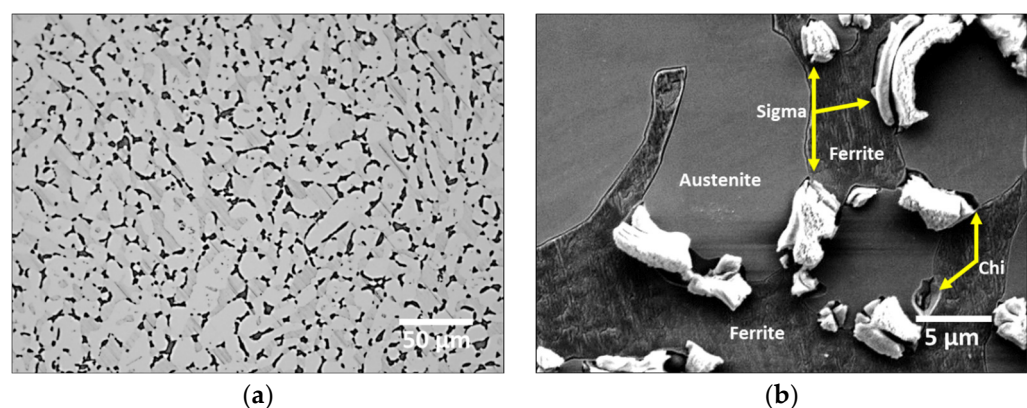
balance resulted in both phases approaching PRE 42, which contributes to the mitigation of galvanic corrosion [12,32].

(a)   (b)

Figure 2. Microstructure of super-duplex stainless steel SAF2507. (**a**) Cast. (**b**) Solution-annealed at 1100 °C (γ: austenite, and δ: ferrite).

3.2. Crystallization of Secondary Phase

The secondary phase precipitates at the boundaries between austenite and ferrite; the microstructure was examined after heat treatment at 1000 °C. After heat treatment at 1000 °C, the precipitation of the secondary phase at the boundaries of austenite was confirmed (Figure 3). The morphology of the secondary phase is indicated by the black dots in Figure 3a. However, the formation of the base structures of ferrite and austenite on the top was observed at higher magnifications (Figure 3b). The secondary phase grew along the grain boundaries of austenite and was observed in two forms: after etching the highly corrosion-resistant microstructure and after etching the microstructure with a relatively low corrosion resistance. The chemical compositions were verified and are listed in Table 3 [33,34]. The two types of secondary phases exhibited differences in their chemical compositions. The highly corrosion-resistant microstructure had a high Cr and Mo chemical composition, whereas that with low corrosion resistance had a low Cr and Mo chemical composition. According to the literature, the highly corrosion-resistant phase is known as Cr-rich Sigma, whereas that with a low corrosion-resistant phase is known as Cr-deficient Chi.
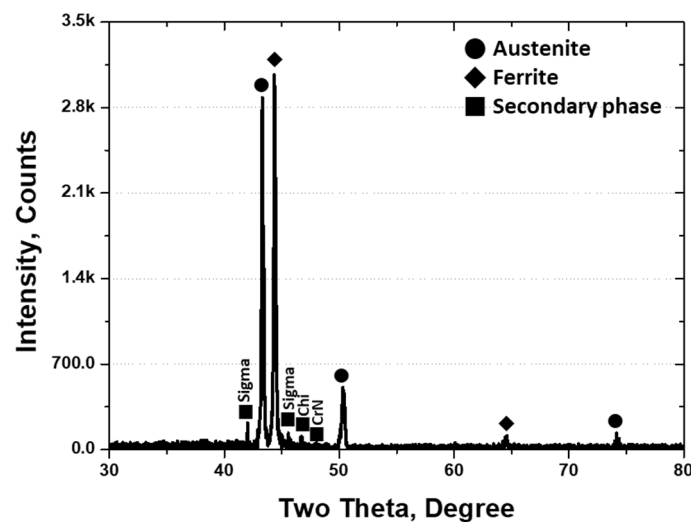

(a)   (b)

Figure 3. Microstructure of super-duplex stainless steel SAF2507 after heat treatment at 1000 °C. (**a**) Magnification ×200. (**b**) Magnification ×5000 (Yellow allows is secondary phase (Sigma, and chi)).

Table 3. The chemical composition of the secondary phase crystallized at the grain boundaries of austenite on super-duplex stainless steel after heat treatment at 1000 °C during 1 h. Unit: wt.%.

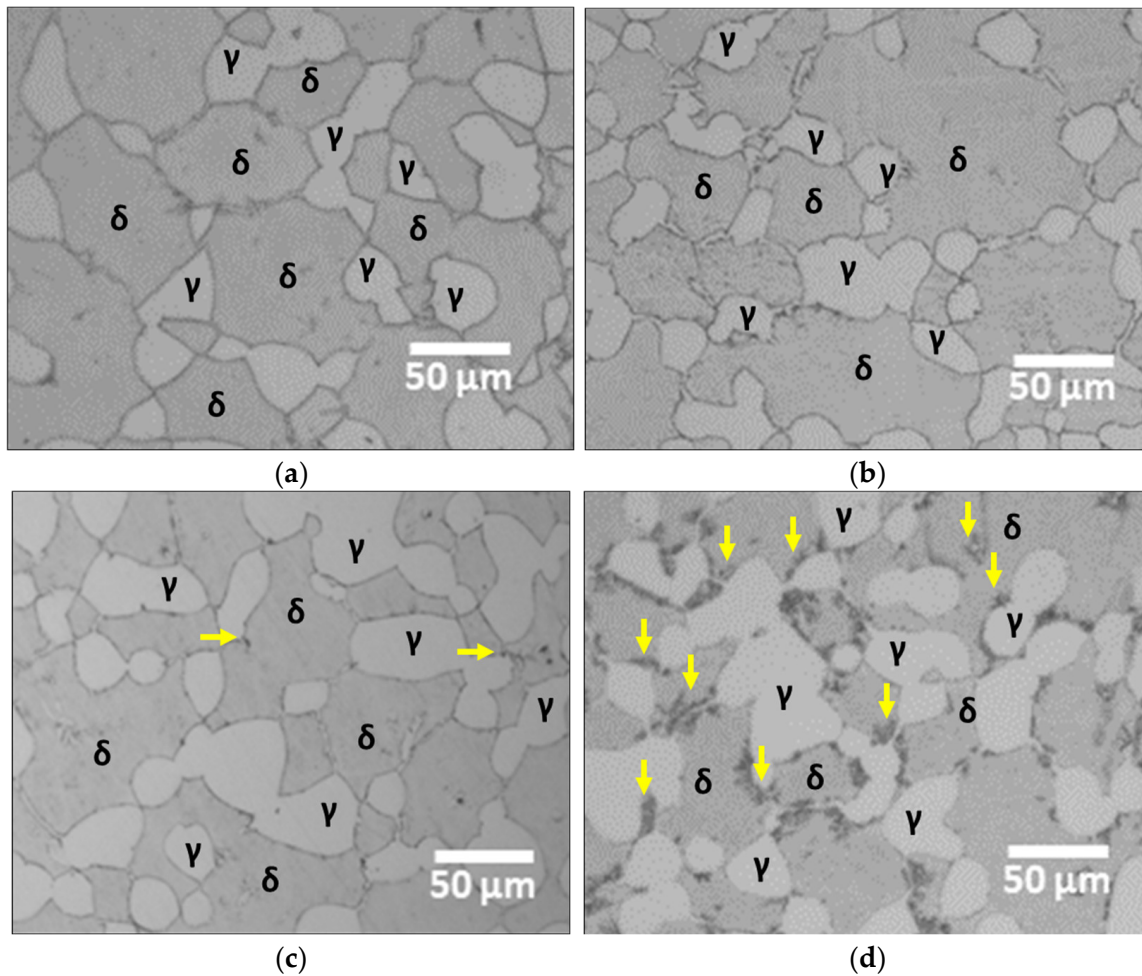| Element	Cr	Mo	Ni	Mn	Fe
Sigma	30.9 ± 1.5	8.9 ± 2.1	4.5 ± 0.8	0.5 ± 0.1	56.3
Chi	22.1 ± 0.9	2.2 ± 0.5	9.5 ± 1.2	1.0 ± 0.2	65.2

XRD patterns provide information on the phases based on the patterns of the diffraction angles, allowing for the determination of the presence of secondary phases. XRD analysis identifies secondary phases as Sigma, Chi, and CrN [29,35]. Although Sigma and Chi were easily distinguishable phases, CrN (size of 0.2 μm) precipitated in fine spherical forms, making it less discernible using FE-SEM analyses. CrN was formed owing to the combination of unalloyed N and Cr during the precipitation of the secondary phase, primarily at the boundaries of the secondary phase. The XRD results show the peaks and intensities of the secondary phase (Figure 4). Owing to its irregular morphology, the secondary phase exhibited XRD peaks of low intensity. Secondary phases were observed at 42°, 46°, 47°, and 48°. The peaks at 42° and 46° corresponded to Sigma, 47° to Chi, and 48° to CrN. Therefore, the secondary phase of SAF2507 was divided into three phases with low intensities.

Figure 4. Intensity (Counts) vs Two theta (Degree) curve, X-ray diffraction pattern after heat treatment at 1000 °C of super-duplex stainless steel SAF2507.

3.3. Secondary Phase at 700 °C

Figure 5 shows the precipitation of the secondary phase after heat treatment at 700 °C for 0–10 h [36,37]. The secondary phase was observed as black dots at low magnification; no precipitation of the secondary phase was observed until 5 h of heat treatment. After 5 h of heat treatment, the secondary phase was observed as black dots (yellow arrows); however, after heat treatment for 10 h, the secondary phase was observed as black lines. As heat-treatment time increased, the volume fraction of the secondary phase increased. Sufficient energy for the phase transformations of austenite, ferrite, and the secondary phase was provided by heat treatment at 700 °C, enabling the crystallization of the secondary phase.

After examining the microstructure of SAF2507 at 700 °C for varying periods of time, the phase fractions were analyzed; the results are presented in Table 4. Prior to the precipitation of the secondary phase at 700 °C, the fractions of austenite and ferrite exhibited minimal changes (less than 0.5%). However, with an increase in the annealing time to 5 and 10 h, the fraction of austenite increased to 27.1% and 31.6%, respectively. Additionally, the ferrite fraction decreased to 60.3%, and the secondary-phase fraction increased to 8.1%. The secondary phase grew along the grain boundaries of austenite.

Figure 5. Microstructure (γ: austenite, and δ: ferrite) with heat treatment time at 700 °C of super duplex stainless steel SAF2507. (**a**) 0 h (before heat treatment). (**b**) 1 h. (**c**) 5 h. (**d**). 10 h (yellow point is secondary phase).

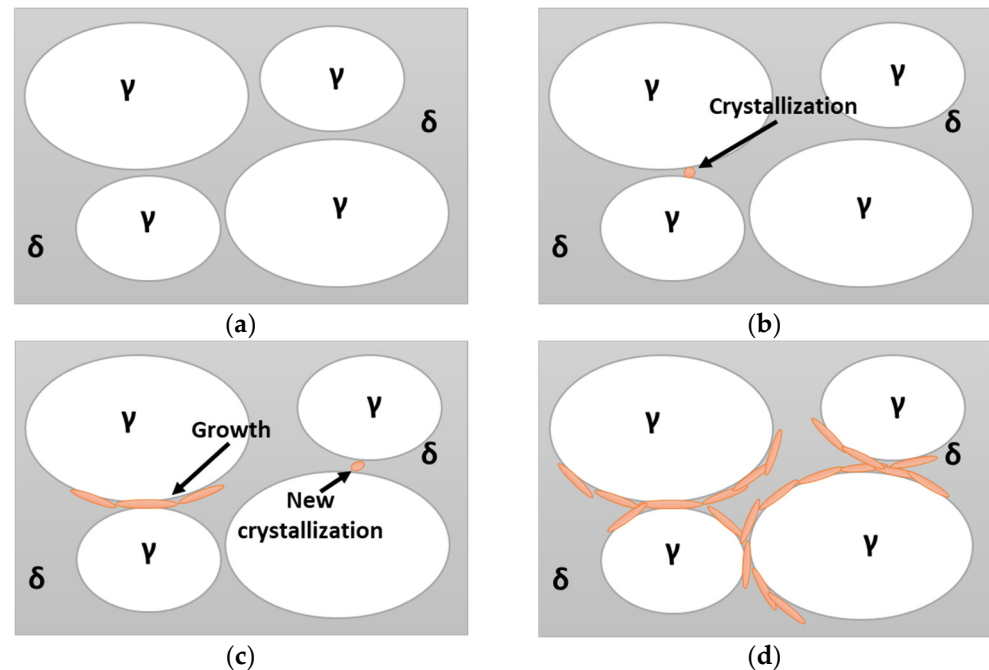**Table 4.** Volume fraction with heat-treatment time at 700 °C of super-duplex stainless steel SAF2507.

Heat Treatment Time	0 h	1 h	5 h	10 h
Austenite	25.5 ± 2.3%	25.4 ± 2.1%	27.1 ± 2.0%	31.6 ± 1.9%
Ferrite	74.5 ± 2.3%	74.6 ± 2.1%	71.9 ± 2.0%	60.3 ± 2.2%
Secondary phase	0.0 ± 0.0%	0.0 ± 0.0%	1.0 ± 0.6%	8.1 ± 1.8%

The precipitation and crystallization behavior of the secondary phase exhibited a common crystallization characteristic at the boundaries of austenite when crystallized at high (1000 °C) and low (700 °C) temperatures. However, there were differences in the growth of the secondary phases. At 1000 °C, the secondary phase crystallized and grew within an hour. In contrast, the secondary phase did not precipitate after 1 h of annealing at 700 °C; however, precipitation was observed after 5 h. Previous studies have suggested that the precipitation of the secondary phase is facilitated by the segregation of Cr and Mo owing to the growth of austenite. However, the precipitation of the secondary phase was observed at 700 °C after annealing, even without the segregation of Cr and Mo.

3.4. Crystallization Behavior of the Secondary Phase

The crystallization of the secondary phase occurred at the grain boundaries between austenite and ferrite. The ease of crystallization was greater in areas with higher austenite volume fractions. The crystallization of the secondary phase and its subsequent growth are

shown in Figure 6. Initially, the crystallization of the secondary phase, in which the two austenite regions were in close proximity, was observed. Subsequently, the existing crystals grew along the boundaries of the enlarged austenite and formed new crystallization sites. Crystallization of the secondary phase continued progressively at each site. In addition, the crystallization and growth of the secondary phase were observed even when the volume fraction of austenite was less than 50%.

Figure 6. Schematic diagram of crystallization and growth on super-duplex stainless steel SAF2507. (**a**) Before crystallization. (**b**) Crystallization of the secondary phase occurs easily when two austenites are in close proximity. (**c**) Secondary-phase crystalline growth along the boundary of the austenite. (**d**) Growth of the secondary phase.

A crystallized secondary phase at 1000 °C was observed when the volume fraction of austenite was higher than 58%, whereas crystallization of the secondary phase occurred at 700 °C when the volume fraction of austenite exceeded 27%. This difference significantly influenced the crystallization of the secondary phase. Previous studies have shown that the crystallization of the secondary phase started with Sigma and subsequently proceeded to Chi. Because Sigma has a high chemical composition of Cr and Mo, these elements play crucial roles in its crystallization. Therefore, sites conducive to alloy segregation at the grain boundaries of austenite act as sites for Sigma crystallization at 700 °C owing to the ease of major alloy segregation, which facilitates Sigma crystallization.

4. Discussion

To enhance the stability of the case materials of Li-ion batteries, the fever temperature of the battery was increased to 700 °C, and the crystallization behavior of the secondary phase was observed [14,25]. The secondary phase crystallized, precipitated at the austenite boundaries, and grew along the grain boundaries. The crystallization and growth behaviors of the secondary phase are shown in Figure 6. The secondary phase grew along the austenite boundaries. After heat treatment at 700 °C for 10 h, the volume fraction of the secondary phase increased to 8.1%. During this process, the volume fraction of austenite increased by 6%, whereas that of ferrite decreased by 14%. Growth predominantly occurred in the ferrite direction, which had a higher chemical composition of Cr and Mo, contributing to a decrease in the volume fraction of ferrite. Changes in the austenite morphology indicate

variations in volume fractions, and the measured volume fractions enable the assessment of phase transformations from ferrite to austenite and the secondary phase.

Even with volume fractions of austenite below 26%, the grain boundaries of austenite that are susceptible to phase transformation tend to segregate the chemical composition, such as Cr and Mo [30,37]. Therefore, the area with increased volume fractions of austenite (the site of phase transformation) facilitated greater precipitation and crystallization of the secondary phase. The sites prone to ferrite transformation exhibited favorable conditions for the crystallization and growth of the secondary phase because of the segregation of major alloying elements such as Cr and Mo.

Although the precipitation and crystallization of the secondary phase from the heat generated by the Li-ion battery reaction using SAF2507 were feasible at 700 °C, it required more than 5 h, and the fraction of the secondary phase remained low. Hence, the application of SAF2507 as a case material for Li-ion batteries can enhance battery stability because of the inhibited crystallization and growth of the secondary phase [1,7,38].

The results of this study were discussed and interpreted from the perspective of previous studies and working hypotheses. We also highlighted prospects for further studies. These findings and their implications should be discussed in the broadest possible context.

5. Conclusions

To apply SAF2507 as a case material for Li-ion batteries and assess its effect on the secondary-phase crystallization at 700 °C, the following findings were summarized:

1. SAF2507 precipitated at 1000 °C. Secondary-phase crystallization was initiated when the transformation of austenite from ferrite occurred at the austenite boundary. Because ferrite possessed a higher Cr content (26.6 wt.%) than austenite (23.3%), the transformation of ferrite to austenite resulted in the transfer of Cr (>3%) to ferrite. This led to the crystallization of the secondary phase owing to the unallocated Cr content. The crystallized secondary phase grew along the austenite boundaries.
2. SAF2507 was heat-treated over time at the operating temperature of Li-ion batteries (700 °C). After 5 h of treatment, secondary-phase crystallization was observed; this reached 8.1% after 10 h of heat treatment. The crystallization of the secondary phase was initiated at the boundaries of austenite owing to the differences in crystallization and the high energy required for phase transformation.
3. SAF2507 exhibited excellent strength and corrosion resistance. The crystallization of the secondary phase occurred after heat treatment for 5 h at 700 °C. As the operating time of a Li-ion battery is less than 5 h, secondary-phase crystallization is unlikely to occur. The safety of using Li-ion batteries at operating times beyond 5 h at 700 °C due to improved performance is expected to be maintained before the crystallization of the secondary phase occurs. Therefore, the use of SAF2507 as the material for Li-ion battery cases has the potential to enhance safety against high-temperature fever and damage.

References

1. Mayyas, A.; Steward, D.; Mann, M. The Case for Recycling: Overview and Challenges in the Material Supply Chain for Automotive Li-Ion Batteries. *Sustain. Mater. Technol.* **2019**, *19*, e00087. [CrossRef]
2. Rahman, A.; Lin, X. Li-Ion Battery Individual Electrode State of Charge and Degradation Monitoring Using Battery Casing through Auto Curve Matching for Standard CCCV Charging Profile. *Appl. Energy* **2022**, *321*, 119367. [CrossRef]
3. Tudoroiu, R.-E.; Zaheeruddin, M.; Tudoroiu, N.; Radu, S.M.; Chammas, H. Investigations of Different Approaches for Controlling the Speed of an Electric Motor with Nonlinear Dynamics Powered by a Li-Ion Battery-Case Study. In *Electric Vehicles—Design, Modelling and Simulation*; IntechOpen: London, UK, 2023.
4. Klink, J.; Hebenbrock, A.; Grabow, J.; Orazov, N.; Nylén, U.; Benger, R.; Beck, H.-P. Comparison of Model-Based and Sensor-Based Detection of Thermal Runaway in Li-Ion Battery Modules for Automotive Application. *Batteries* **2022**, *8*, 34. [CrossRef]
5. Tudoroiu, N.; Zaheeruddin, M.; Tudoroiu, R.-E.; Radu, M.S.; Chammas, H. Investigations on Using Intelligent Learning Techniques for Anomaly Detection and Diagnosis in Sensors Signals in Li-Ion Battery—Case Study. *Inventions* **2023**, *8*, 74. [CrossRef]
6. Park, J.; Fatima, S.A. A DFT Study of TiC3 as Anode Material for Li-Ion Batteries. *Appl. Surf. Sci.* **2023**, *638*, 158024. [CrossRef]
7. Kale, R.B.; More, S.S.; Khupse, N.D.; Kalubarme, R.S.; Kulkarni, M.V.; Rane, S.B.; Kale, B.B. High-Voltage Ionic Liquid-Based Flexible Solid Polymer Electrolyte for High-Performance Li-Ion Batteries. *Sustain. Energy Fuels* **2023**, *7*, 2934–2942. [CrossRef]
8. Hoosain, S.E.; Tshabalala, L.C.; Skhosana, S.; Freemantle, C.; Mndebele, N. Investigation of the Properties of Direct Energy Deposition Additive Manufactured 304 Stainless Steel. *S. Afr. J. Ind. Eng.* **2021**, *32*, 258–263. [CrossRef]
9. Yoo, Y.-R.; Choi, S.-H.; Kim, Y.-S. Effect of Laser Peening on the Corrosion Properties of 304L Stainless Steel. *Materials* **2023**, *16*, 804. [CrossRef] [PubMed]
10. Acharyya, S.G.; Khandelwal, A.; Kain, V.; Kumar, A.; Samajdar, I. Surface Working of 304L Stainless Steel: Impact on Microstructure, Electrochemical Behavior and SCC Resistance. *Mater. Charact.* **2012**, *72*, 68–76. [CrossRef]
11. Speidel, M.O. Nitrogen Containing Austenitic Stainless Steels. *Mater. Werkst. Entwickl. Fert. Prüfung Eig. Anwendungen Tech. Werkst.* **2006**, *37*, 875–880. [CrossRef]
12. Ha, H.-Y.; Lee, T.-H.; Bae, J.-H.; Chun, D.W. Molybdenum Effects on Pitting Corrosion Resistance of FeCrMnMoNC Austenitic Stainless Steels. *Metals* **2018**, *8*, 653. [CrossRef]
13. Nishimoto, M.; Muto, I.; Sugawara, Y. Review—Understanding and Controlling the Electrochemical Properties of Sulfide Inclusions for Improving the Pitting Corrosion Resistance of Stainless Steels. *Mater. Trans.* **2023**, *64*, 2051–2058. [CrossRef]
14. Nilsson, J.-O. Super Duplex Stainless Steels. *Mater. Sci. Technol.* **1992**, *8*, 685–700. [CrossRef]
15. Sung, C.; Shin, B.-H.; Chung, W. Effect of Solution Annealing on Austenite Morphology and Pitting Corrosion of Super Duplex Stainless Steel UNS S 32750. *Int. J. Electrochem. Sci.* **2021**, *16*, 210813. [CrossRef]
16. Martins, M.; Casteletti, L.C. Sigma Phase Morphologies in Cast and Aged Super Duplex Stainless Steel. *Mater. Charact.* **2009**, *60*, 792–795. [CrossRef]
17. Baghdadchi, A.; Hosseini, V.A.; Valiente Bermejo, M.A.; Axelsson, B.; Harati, E.; Högström, M.; Karlsson, L. Wire Laser Metal Deposition of 22% Cr Duplex Stainless Steel: As-Deposited and Heat-Treated Microstructure and Mechanical Properties. *J. Mater. Sci.* **2022**, *57*, 9556–9575. [CrossRef]
18. Moniruzzaman, F.N.U.M.; Shakil, S.I.; Shaha, S.K.; Kacher, J.; Nasiri, A.; Haghshenas, M.; Hadadzadeh, A. Study of Direct Aging Heat Treatment of Additively Manufactured PH13–8Mo Stainless Steel: Role of the Manufacturing Process, Phase Transformation Kinetics, and Microstructure Evolution. *J. Mater. Res. Technol.* **2023**, *24*, 3772–3787. [CrossRef]
19. Sung, C.; Shin, B.-H.; Chung, W. Effect of Heat Energy Input on Electrochemical Properties of Solution-Annealed Super-Duplex Stainless Steel UNS S 32750 Laser Welding. *Int. J. Electrochem. Sci.* **2022**, *17*, 220339. [CrossRef]
20. Sung, C.; Kim, K.; Chung, W.; Shin, B.-H. Electrochemical Properties of UNS S 32750 and UNS S 32760 Annealed Super Duplex Stainless Steels. *Int. J. Electrochem. Sci.* **2022**, *17*, 220526. [CrossRef]
21. Valiente Bermejo, M.A.; Thalavai Pandian, K.; Axelsson, B.; Harati, E.; Kisielewicz, A.; Karlsson, L. Microstructure of Laser Metal Deposited Duplex Stainless Steel: Influence of Shielding Gas and Heat Treatment. *Weld. World* **2021**, *65*, 525–541. [CrossRef]
22. Paulraj, P.; Garg, R. Effect of Intermetallic Phases on Corrosion Behavior and Mechanical Properties of Duplex Stainless Steel and Super-Duplex Stainless Steel. *Adv. Sci. Technol. Res. J.* **2015**, *9*, 87–105. [CrossRef] [PubMed]
23. Topolska, S.; Łabanowski, J. Effect of Microstructure on Impact Toughness of Duplex and Superduplex Stainless Steels. *J. Achiev. Mater. Manuf. Eng.* **2009**, *36*, 142–149.
24. Linton, V.M.; Laycock, N.J.; Thomsen, S.J.; Klumpers, A. Failure of a Super Duplex Stainless Steel Reaction Vessel. *Eng. Fail Anal.* **2004**, *11*, 243–256. [CrossRef]
25. Tehovnik, F.; Arzensek, B.; Arh, B.; Skobir, D.; Pirnar, B.; Zuzek, B. Microstructure Evolution in SAF 2507 Super Duplex Stainless Steel. *Mater. Technol.* **2011**, *45*, 339–345.
26. Elhoud, A.M.; Renton, N.C.; Deans, W.F. Hydrogen Embrittlement of Super Duplex Stainless Steel in Acid Solution. *Int. J. Hydrogen Energy* **2010**, *35*, 6455–6464. [CrossRef]
27. Vongsilathai, S.; Lothongkum, A.W.; Lothongkum, G. Corrosion Behavior of a New 25Cr-3Ni-7Mn-0.66 N Duplex Stainless Steel in Artificial Seawater. *Mater. Test.* **2021**, *63*, 505–511. [CrossRef]
28. Shin, B.-H.; Park, J.; Jeon, J.; Heo, S.; Chung, W. Effect of Cooling Rate after Heat Treatment on Pitting Corrosion of Super Duplex Stainless Steel UNS S 32750. *Anti-Corros. Methods Mater.* **2018**, *65*, 492–498. [CrossRef]

29. Shin, B.-H.; Park, J.; Kim, S.; Ok, J.-W.; Kim, D.-I.; Yoon, J.-H. Study of Electroless Nickel Plating on Super Duplex Stainless Steel for Lithium-Ion Battery Cases: Electrochemical Behaviour and Effects of Plating Time. *Metals* **2024**, *14*, 307. [CrossRef]

30. Pettersson, N.; Pettersson, R.F.A.; Wessman, S. Precipitation of Chromium Nitrides in the Super Duplex Stainless Steel 2507. *Metall. Mater. Trans. A* **2015**, *46*, 1062–1072. [CrossRef]

31. Oh, S.; Kim, D.; Kim, K.C.; Kim, D.-I.; Chung, W.; Shin, B.-H. Electrochemical Properties of Electroless Ni Plated Super Duplex Stainless in 3.5% NaCl Solution. *Int. J. Electrochem. Sci.* **2023**, *18*, 100287. [CrossRef]

32. Nilsson, J.O.; Wilson, A. Influence of Isothermal Phase Transformations on Toughness and Pitting Corrosion of Super Duplex Stainless Steel SAF 2507. *Mater. Sci. Technol.* **1993**, *9*, 545–554. [CrossRef]

33. Kannan, A.R.; Shanmugam, N.S.; Rajkumar, V.; Vishnukumar, M. Insight into the Microstructural Features and Corrosion Properties of Wire Arc Additive Manufactured Super Duplex Stainless Steel (ER2594). *Mater. Lett.* **2020**, *270*, 127680. [CrossRef]

34. Maurya, A.K.; Pandey, C.; Chhibber, R. Effect of Filler Metal Composition on Microstructural and Mechanical Characterization of Dissimilar Welded Joint of Nitronic Steel and Super Duplex Stainless Steel. *Arch. Civ. Mech. Eng.* **2022**, *22*, 90. [CrossRef]

35. Valeriano, L.D.C.; Correa, E.O.; Mariano, N.A.; Robin, A.L.M.; Machado, M.A.G. Influence of the Solution-Treatment Temperature and Short Aging Times on the Electrochemical Corrosion Behaviour of Uns S32520 Super Duplex Stainless Steel. *Mater. Res.* **2019**, *22*, e20180774. [CrossRef]

36. Kim, D.; Chung, W.; Shin, B.-H. Effects of the Volume Fraction of the Secondary Phase after Solution Annealing on Electrochemical Properties of Super Duplex Stainless Steel UNS S32750. *Metals* **2023**, *13*, 957. [CrossRef]

37. Shin, B.-H.; Kim, D.; Park, S.; Hwang, M.; Park, J.; Chung, W. Precipitation Condition and Effect of Volume Fraction on Corrosion Properties of Secondary Phase on Casted Super-Duplex Stainless Steel UNS S32750. *Anti-Corros. Methods Mater.* **2018**, *66*, 61–66. [CrossRef]

38. Shin, B.-H.; Kim, D.; Kim, D.-I.; Lee, W.; Kwon, S.-H. Effect of Microstructure on Electroless Ni Plating Behavior on Super Duplex Stainless Steel SAF2507 in Li-Ion Batteries. *Coatings* **2023**, *13*, 1807. [CrossRef]